Check for
updates

Optical properties and far field radiation of periodic nanostructures fed by an optical waveguide for applications in fluorescence and Raman scattering

Badrul Alam[1] · Antonio Ferraro[2,3] · Roberto Caputo[2,3] · Rita Asquini[1]

Abstract

Various systems based on nanostructures built on optical waveguides have recently appeared in literature, since this configuration guarantees an efficient optical feeding to nano-elements and/or the possibility to manipulate guided signals. In this work, we present the analysis of the optical scattering properties of such type of structures, more specifically a periodic array of Au nano-cylinders or nano-domes fabricated upon an ion-exchanged waveguide, an integrated system considered for fluoroscopy and Raman spectroscopy. Absorption, scattering and extinction were calculated by means of Finite Difference Time Domain (FDTD) simulations and Scattering Theory. We took advantage of some particular adaptations to apply the classical scattering theory to this context, and used it to extract the far-field radiation pattern. We show that the rectangular periodicity allows to obtain highly collimated beams and negligible irradiation in a wide angle range, which enables the possibility to steer away the undesirable excitation signals from the detectors, avoiding a mixing with emitted photons from molecules. Our analysis suggests that, in the context of this setup and applications, the modeling of the nanostructures, which aims at the tuning of the plasmonic enhancement of the emission, can be relatively separated from the definition of spatial filtering through the periodic array. Our results add new considerations to the list of potentialities of this configuration for the development of efficient integrated surface enhanced spectroscopic setups.

✉ Rita Asquini
  rita.asquini@uniroma1.it

1   Department of Information Engineering, Electronics and Telecommunications, Sapienza University of Rome, Rome, Italy

2   Department of Physics, University of Calabria, Cosenza, Italy

3   Consiglio Nazionale delle Ricerche - Istituto di Nanotecnologia (CNR-Nanotec), 87036 Rende, Italy

⌖ Springer

1 Introduction

Optical nanostructures have been widely studied in the last decade, and their development is still in progress, due to the several applications they enable (Thomas et al. 2020; Kasani et al. 2019). In particular, metal based nanoelements have shown great potential, since the Surface Plasmon Polaritons (SPPs) emerging from the metal/dielectric interfaces are capable of producing unique phenomena, that have been exploited in various fields and for many purposes (Maier 2010).

Most of the nanostructures in literature are designed for applications requiring a free-space spectroscopic setup (Yu et al. 2019; Veroli et al. 2019). In these cases, the nano-structures are fabricated upon samples that will be part of the setup. Usually, in order to reduce costs and complexity, nanostructures are built in small areas of the overall substrate, and a relevant effort is required to convey the laser light in the desired region and/or in the control of the spot size. For those operations, expertise and manual control over the free-space optical instrumentation is required, and this is a limit to the applications of the nanostructures. On the other hand, adopting optical setups with a fixed alignment requires little or no direct handling from operators, although at the cost of needing samples with a wide coverage area from the nanostructures, which corresponds to higher fabrication costs and complexity.

Recently, a trend towards the fabrication of nanostructures upon optical waveguides is gaining popularity in literature (Tian et al. 2019; Calò et al. 2019; Dhakal et al. 2016; Buzzin et al. 2021). This configuration is mostly used for two kinds of situations: it allows to feed the optical nanostructures without requiring the aforementioned complex alignment processes, or it is used for some specific manipulation of the signal traveling on the waveguides in the optical integrated circuits.

The integration of platforms on a waveguide can be innovative in the fields of Fluorescence and Raman Spectroscopy (Sultangaziyev et al. 2020; Larkin 2017). Roughly speaking, in both applications the evolution of the signal is similar (despite involving different physical phenomena): an excitation light illuminating molecules/cells induces their emission of light at a higher wavelength. By reading the emitted signal, in particular the related color and response time, it is possible to determine some specific characteristics of the objects under study. In this scenario, plasmonic nanostructures are often used close to the emitters due to the capacity to enhance their emissions (with proper conditions or design). While most of the literature on the topic is related to free space optical setup, some recent works have shown the potentialities of the waveguide based setup (Tian et al. 2019; Dhakal et al. 2016), where metallic nanostructures were employed as anchor for the molecules and for their emission enhancement. Despite those works proved some of the advantages of this approach, their study focused mainly on the relation between the emitted signals and the single nanostructures, and did not describe in depth the relation between the excitation signal and the overall group of nanostructures, in particular when involving arrays, even though it is an integral component of the system.

In this work, we analyze the scattering parameters of a periodic nano-array fed by the evanescent fields of light propagating through an ion-exchanged graded-index waveguide, and subsequently we perform the calculation of the directivity of such a system. Our study involves different geometries, nanoscopic cylinders and domes, with the intent of determining the general characteristics of the configuration in the context of an integrated optical setup for fluorescence and Raman spectroscopy. As shown previously (Alam et al. 2021), the analysis requires some approximations in the general formulation of Scattering theory,

which we show here in greater detail. We used the obtained scattered fields to extract the far field radiation pattern. After describing the numerical-analytical model, we proceeded with their application on the nano-cylinders and nano-domes. In order to gain insight of the behavior of this system in the context of the applications in Fluorescence and Raman scattering, our analysis includes the comparison between the two geometries, and the relation of the parameters with the array period.

This manuscript is articulated as follows. In Sect. 2, the physical characteristics of the optical structure and the working principles are described, as well as the simulation setups. In Sect. 3, the scattering parameter analysis formulation in the classical description and in the new situations is presented, with details of the issues and related approximations. In Sect. 4, the calculation of the far-field radiation properties is shown. In Sect. 5, we discuss the results and we discern the implications on the design of integrated spectroscopic setups. In the final section, the conclusions are drawn.

2 Optical structure and working principle

The system under study, presented in Fig. 1, consists of an array of Au nanostructurs, either cylinders or dome shaped, built on an ion-exchanged waveguide. Such a structure is interesting for phenomena such as enhancement of fluorescence, surface enhanced Raman
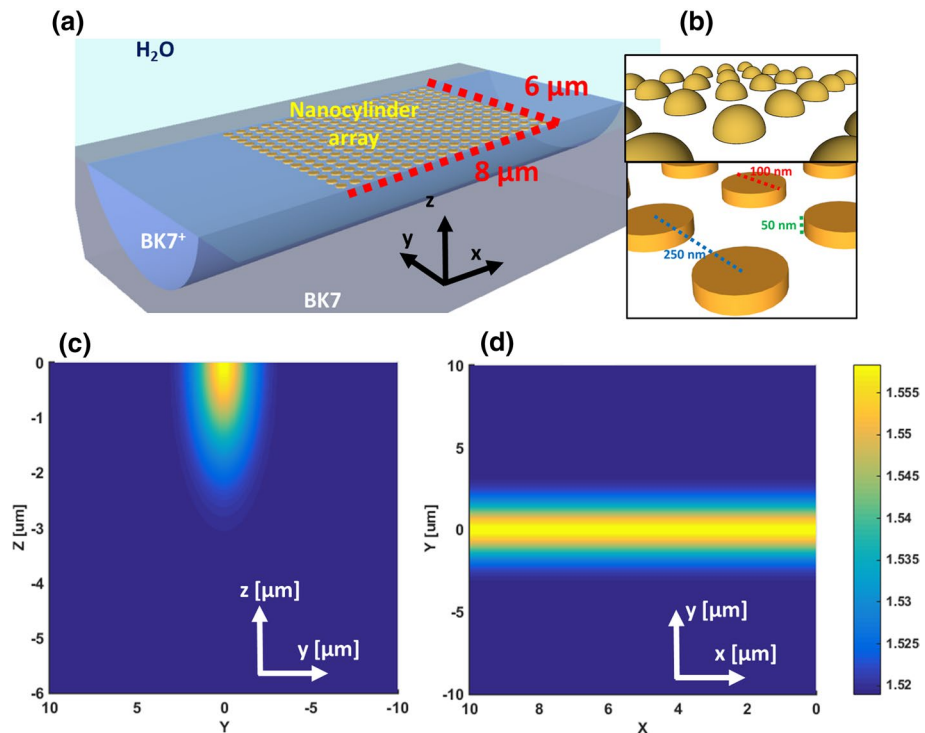

Fig. 1 a Schematic view of the structure under analysis. **b** Details of the nano-array. **c** and **d** refractive index profile of the waveguides in the transversal and longitudinal directions, respectively

Spectroscopy, etc. In this system, the nano-array is used as an anchor to specific molecules, and as an enhancement antenna (through SPPs) for their emission. The waveguide is used as a power feed for the excitation from nano-array and the molecules.

In this system, the waveguide and the nano-array are expected to be exposed to a solution rich of water with small content of other organic elements ($n \approx 1.3$), which will be considered the upper cladding. The waveguide is developed on a substrate of BK7 glass, and has been obtained through a double ion-exchange in a melt of KNO_3 and $AgNO_3$ (Zou et al. 2002; Asquini et al. 2018), which results in a graded index profile that follows the shape of a Gaussian distribution (Fig. 1c, d). This type of waveguides is convenient for several reasons. Firstly, the waveguide is embedded in the substrate, meaning an easy fabrication of nano-arrays through Electron Beam Lithography, since a flat glass surface is a preferential substrate. Besides, the modes propagating inside it generate a relevant evanescent field on the top cladding interface. Bottom cladding is the remaining BK7 substrate ($n_{BK7} = 1.519$). The geometrical parameters of the nano-cylinders have been selected to provide fluorescence enhancement, and follow the dimensions previously adopted in other works (Mahi et al. 2017), namely square array with 250 nm array period, 100 nm diameter and 50 nm thick cylinders. On the other hand, the geometry of the nano-domes are inspired from (Choi et al. 2010), with a chosen diameter of 100 nm and 250 nm array period.

In this analysis, simulations have been performed using Finite Difference Time Domain method, implemented in the commercial tool Lumerical (although the concepts of this work can be applied also to other methods). The upper cladding and the bottom cladding have been considered as virtually infinite, thus the "perfectly matched layer" (PML) was chosen as boundary conditions. The waveguide has been obtained by a Gaussian profile with parameters: $n(x,y) = n_{BK7} + \Delta n \cdot e^{-\frac{x^2}{h_x^2}} e^{-\frac{y^2}{h_y^2}}$, where $\Delta n = 0.04$ and $h_x = h_y = 1.549 \, \mu m$ being these last parameters related to the depth of the doping.

The input signal in the graded index waveguide is its fundamental TM_{00} mode, since it is better suited for interaction with the plasmonic elements. In Fig. 2 the field profiles resulting from FDTD simulations are shown. As it can be noticed, the TM_{00} mode travelling through the waveguide is perturbed when its evanescent components ($z > 0$) meet the array of nano-cylinders. While the waveguide alone features negligible propagation loss, the nanostructures either absorb or scatter away a portion of the signal. Thus, a portion of the feeding power is lost at the output of the waveguide.

3 Scattering parameter analysis

3.1 Classical scattering theory

Our analysis of the structure uses an approximation of the scattering theory. It was previously introduced in (Alam et al. 2021), and here it is better represented and articulated. It consists in the simulation of the system with and without objects, the latter situation being a reference. Those simulations are needed to obtain the fields from a surface enclosing the system; in our situation, those consisted in a cubic box of "monitors", i.e. six rectangular 2D planes where field values are recorded (in FDTD, the amounts are time averaged over the duration of the simulation). Thus, from the monitor box we obtain the field distributions: E_m and H_m from the main and E_{ref} and H_{ref} from the reference, which allow to calculate the overall scattering parameters of the enclosed volume, and help to model the relevant internal system as an abstract block. Furthermore, these local field values help to compute the far field radiation
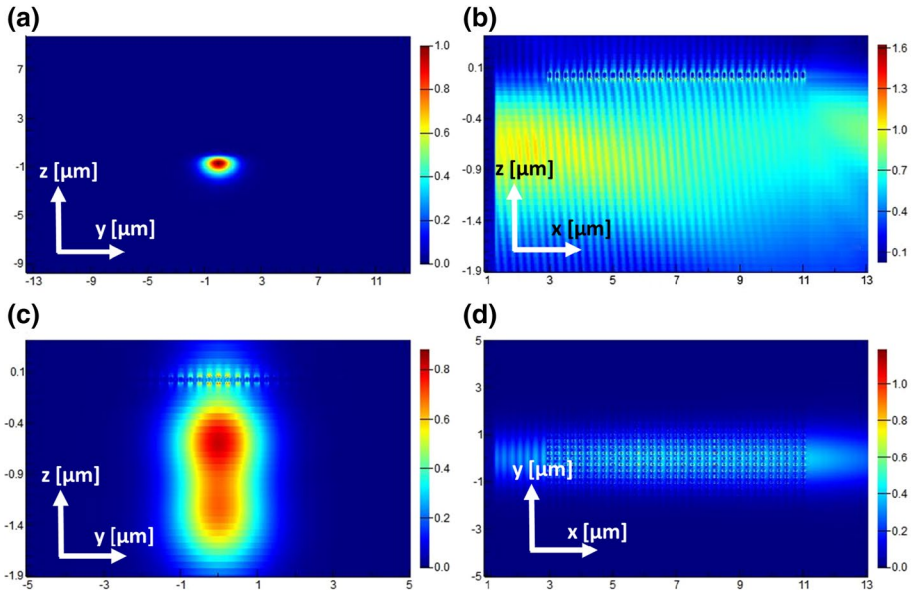
(a)

(b)

(c)

(d)

Fig. 2 Field profiles at the cross-sections of the system under analysis. **a** Transverse view of the TM$_{00}$ mode |E| field distribution at the input. **b** Longitudinal side-view of the waveguide cutting through a column of nano-cylinders. **c** Transverse view of the signal in the middle of the nano-array, cutting through a row of nano-cylinders. **d** Transverse top-view of the evanescent field impinging on the nano-arrays, taken from z = 0.025 μm, which cuts nano-arrays in half

properties. A schematic representation of the cubic monitor box and the simulation volume is represented in Fig. 3a–I, along with the geometrical vectors. The source considered in the general formulation consists usually in a plane wave.

From the main simulations (with "scatterers"), the absorption is calculated through (Bohren et. al., 1983):

$$Re\left(\frac{1}{2}\oint_S \left(\overline{E}_m \times \overline{H}_m^*\right)d\overline{S}\right) = -W_{abs} \tag{1}$$

This comes as a consequence since the enclosed volume is in a passive, non-dispersive and non-absorbent environment. Consequently, in the reference, the total amount of power entering the volume is equal to the power exiting the volume, so absorption of the overall volume is 0. On the other hand, when the objects are present, those either absorb power from the incident field or redirect it in different directions, thus scattering it away. Thus, in this situation the fields in the box monitors are a combination between the scattered field and the source signal that has not interacted with the objects; in other words, this means that the power entering the volume is higher than the power exiting it.

On the box monitors, in general contexts where the absorption is low, is (Bohren et al. 1983):

$$\begin{aligned}\overline{E}_m &= \overline{E}_{ref} + \overline{E}_s \\ \overline{H}_m^* &= \overline{H}_{ref}^* + \overline{H}_s^*\end{aligned} \tag{2}$$
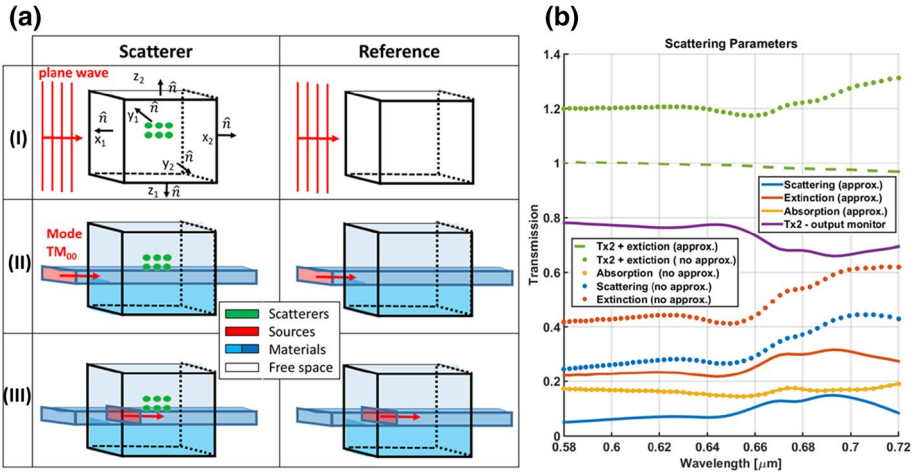
Fig. 3 a Schematic representation of objects of the systems, as perceived by the analytical system in the three different approaches, as taken from (Alam et al., 2021): **(I)** classical configuration, **(II)** waveguide with source outside the box, **(III)** waveguide with source inside the box. **b** Scattering parameters obtained from the calculations of the nano-cylinder, with and without approximation

where $\overline{E}_s$ and $\overline{H}_s$ correspond to scattered field's components. By combining (1) with (2), is possible to obtain:

$$Re\left(\frac{1}{2}\oint_S \left(\overline{E_m} \times \overline{H_m^*}\right)\overline{dS}\right) = -W_{abs}$$

$$Re\left(\frac{1}{2}\oint_S \left(\left(\overline{E_{ref}} + \overline{E_s}\right) \times \left(\overline{H_{ref}^*} + \overline{H_s^*}\right)\right)\overline{dS}\right) = -W_{abs}$$

$$\begin{aligned} Re\left(\frac{1}{2}\oint_S \left(\overline{E_{ref}} \times \overline{H_{ref}^*}\right)\overline{dS}\right) + Re\left(\frac{1}{2}\oint_S \left(\overline{E_s} \times \overline{H_s^*}\right)\overline{dS}\right) \\ + Re\left(\frac{1}{2}\oint_S \left(\left(\overline{E_{ref}} \times \overline{H_s^*}\right) + \left(\overline{E_s} \times \overline{H_{ref}^*}\right)\right)\overline{dS}\right) = -W_{abs} \end{aligned} \tag{3}$$

The first addend is 0 because of the aforementioned reasons, while the second addend refers to the scattered field, W_s. The third addend is generally indicated as the extinction, $-W_{ext}$. With those new definitions, (3) can be reordered in:

$$W_{ext} = -Re\left(\frac{1}{2}\oint_S \left(\left(\overline{E_{ref}} \times \overline{H_s^*}\right) + \left(\overline{E_s} \times \overline{H_{ref}^*}\right)\right)\overline{dS}\right) = W_s + W_{abs} \tag{4}$$

So, overall, the extinction defines the total amount of the signal that has interacted with the objects. Depending on the situation, Eqs. (1)–(4) are used to obtain the desired scattering parameters or to isolate the field monitors for scattered field.

Computationally, the closed-surface-integrals can be obtained from the sum of the power flowing through each monitor, which is obtained either with an integral function or with the sum of Poynting vectors of the monitor points after a weighting of the mesh areas.

3.2 Feeding waveguide—outside source

The situation with a feeding waveguide and the scatterers is presented in Fig. 3a-II, and consists in various non idealities as compared to the standard situation. Firstly, there are different interfaces in the system, in particular the top cladding (water) and the bottom cladding (glass). Moreover, there are intersections between the feeding waveguides and the box monitors, and most of the remaining box surface is not affected by the input power.

Considering the waveguide as lossless, which is approximately true for the majority of technologies, in the reference it is possible to consider $Re\left(\frac{1}{2}\oint_S\left(\overline{E_{ref}}\times\overline{H_{ref}^*}\right)\overline{dS}\right) = 0$, as previously assumed in the classical situation. Equation (1) is always perfectly valid, and computes the absorbed power with great precision. On the other hand, trying to apply directly (2)–(4) to the main simulations, anomalies can be found, as shown in Fig. 3b in the "non approximated" curves, where the sum between transmitted power and extinction yields a value greater than 1, which is unreasonable. The main reason is given by the fact that (2) is not valid in the intersection with the waveguides, since in those areas the subtraction between the reference and the main components yields not only the scattered field, but also components from W_{abs} and other monitors' scattered power. We can better represent this situation through a formula, by first defining P_{in} and P_{out} as the input and output powers flowing through the waveguides when intersecting with monitors X1 and X2, respectively. Monitors X1 and X2 are also crossed by the scattered field. The other monitors, Y1,2 and Z1,2, are crossed mainly by the scattered power.

$$P_{in} - P_{scattX1} = W_{abs} + \sum P_{s_{scattY1},Y2,Z1,Z2} + P_{out} + P_{scattX2}; \tag{5}$$

where the power flowing through the X1 monitor is $P_{X1} = P_{in} - P_{scattX1}$, and the power flowing through X2 monitor is $P_{X2} = P_{out} + P_{scattX2}$.

In the case under investigation, it is hard to perfectly separate the scattered power from the guided power. Thus, an approximation is used: assume as 0 the scattered power through the area of the waveguide/monitor intersection, and some additional area around it (taking into account of the evanescent field). While in some situations (e.g. when dealing with high index contrast waveguides, that can easily capture this field) this sacrifice may be negligible, in other situations (e.g. with low index contrast waveguides with small sized scatterers) this choice may remove relevant information. Thus, some further adjustments can be given to reduce the approximation effects.

3.3 Feeding waveguide—inside source

Since FDTD solvers allow considering dipolar and unidirectional sources, the waveguide signal source can be positioned within the enclosing box, thus making the box itself an active object (Fig. 3a-III). This way, monitor X1 is not crossed by the source signal, but only by the scattered field.

$$Re\left(\frac{1}{2}\oint_S \left(\overline{E}_m \times \overline{H}_m^*\right)d\overline{S}\right) = W_{source} - W_{abs} \tag{6}$$

With the new approximations, relations in Eq. (2) can again be considered valid. If Equations (2) and (6) are combined, the outcome is again Eq. (4), since the first term of the counterpart of Eq. (3) is equal to W_{source}, which simplifies with the right-hand side of the equation.

Thus, keeping (6) into account, it is possible to process through (2), (4) and (5) to obtain more accurate solutions for the scattering parameters, which are represented in Fig. 3c with full lines. As can be seen from the plot, the sum between the residual power in the waveguide and the extinction (curve called "waveguide output + extinction (approx.)"), the value is almost 1. Since a portion of the scattered field was removed from the calculations, the overall sum is slightly lower than 1.

The monitors of the scattered field, including the approximated version of X2, have been used to obtain the far field properties of the nanostructures with this type of feeding.

3.4 Optical parameters of the two nanostructures

In Fig.4a–b, absorption, scattering and extinction are shown as a function of the wavelength, in configurations containing nano-cylinders and nano-domes, both with array period 250 nm. Nano-cylinders display a higher absorption level than nano-domes, most probably due to the shape with more abrupt variations. The level of scattered power is similar, given the similar cross-section areas. Both geometries display different peak and dip levels, which, added to Fig.2d, suggests that the overall optical parameters are mainly dependent from near field interactions of the elements.
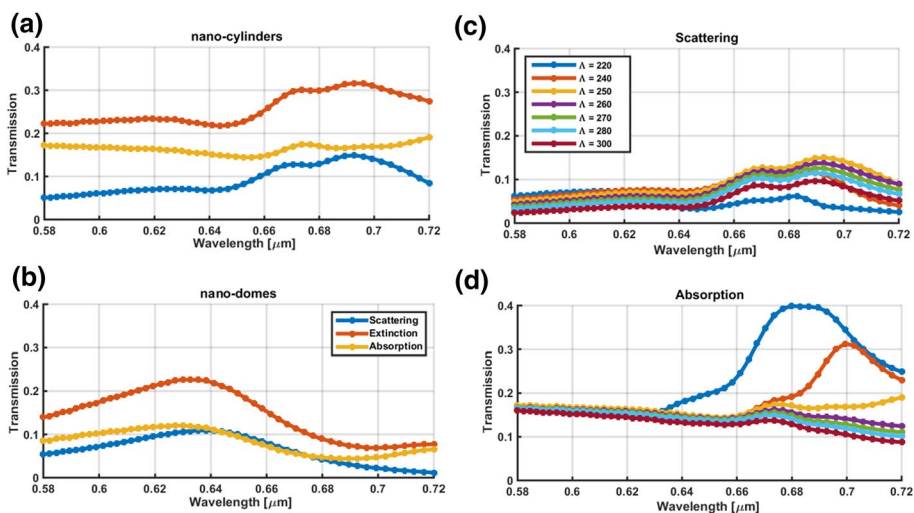

Fig. 4 Optical parameters of the nano-cylinders with parameters {height = 50 nm, radius = 50 nm} and the nanodomes with parameter {radius = 50 nm}. a and b both nanostructures with array period 250 nm. c and d Scattering power and Absorption with nano-cylinders with different array periods, Λ

In Fig.4c–d, the scattering power and absorption are shown, as a function of the wavelength, of the nano-cylinders with different array periods. As can be seen, while the absorption increases with the reduction of the period, most probably due to the increase in number of the lossy nano-cylinders in the same area, the profile of the curves (peak and dips levels) does not change significantly. The decrease of the scattering power along with the array period, which can be related to higher losses along the area, also happen without a significant variation of the curves.

4 Far field radiation diagram

A suitable analytical/numerical tool for the calculation of the Far-Field radiation characteristics starting from the monitor-box scattering field data, is the Stratton-Chu approach (Stratton et al. 1939), later refined and applied in various works (Martin et al. 1998; Benedetti et al. 2014; Centini et al. 2015). While there are various built-in tools in commercial software, in this work, a more explicit approach for the present analysis has been used. In this analysis, evaluation of the $\vec{E}\left(\vec{r}\right)$ field of a set of points, each positioned at $\vec{r}$ was performed, being caused by the points of $\overline{E}_s$ field data in the box-monitors, each positioned at a specific $\vec{r'}$. Subsequently, the computation of the directivity through standard antenna formulas (Balanis 2016) has been executed. The formulas for the calculation of the fields often recall the use of $R = \left|\vec{r} - \vec{r'}\right|$, which is a scalar value, and $\overline{R} = \vec{r} - \vec{r'}$, which is a vector. Also, Green functions $g(R) = \frac{e^{ikR}}{4\pi R}$ are often recalled.

According to classical formulation, the far fields at a position $\vec{r}$ can be obtained through:

$$\begin{cases} \vec{E}\left(\vec{r}\right) = j\omega\mu \int_S \left(\overline{\overline{I}} + \frac{\vec{\nabla}\vec{\nabla}}{k}\right) g(R) * \overline{k}_e\left(\vec{r'}\right) \cdot dS' - \int_S \vec{\nabla} g(R) \times \overline{k}_m\left(\vec{r'}\right) \cdot dS' \\ \vec{H}\left(\vec{r}\right) = j\omega\varepsilon \int_S \left(\overline{\overline{I}} + \frac{\vec{\nabla}\vec{\nabla}}{k}\right) g(R) * \overline{k}_m\left(\vec{r'}\right) \cdot dS' + \int_S \vec{\nabla} g(R) \times \overline{k}_e\left(\vec{r'}\right) \cdot dS' \end{cases} \quad (7)$$

Here, S is the surface of each face of the monitor box, while $\overline{k}_e\left(\vec{r'}\right)$ and $\overline{k}_m\left(\vec{r'}\right)$ are the electric and magnetic fields tangential to the interface, which we will consider as sources of the far-fields. The paramenters ε and μ are respectively the permittivity and the permeability, which, along with the wavenumber k, take into account for the different indeces of the materials that form the claddings.

In the investigated case, the $\vec{E}_s$ and $\vec{H}_s$ field values, at point $\vec{r'}$ are:

$$\begin{aligned} \overline{k}_e\left(\vec{r'}\right) &= +n\left(\vec{r'}\right) \times \vec{H}_s\left(\vec{r'}\right) \\ \overline{k}_m\left(\vec{r'}\right) &= -n\left(\vec{r'}\right) \times \vec{E}_s\left(\vec{r'}\right) \end{aligned} \quad (8)$$

Given the system background environment, it is sufficient to focus the calculations only on one of the field components, for example the E field. Thus, (7) becomes:

$$\vec{E}\left(\vec{r}\right) = 2\int_S g(R)\left(\frac{ikR-1}{R^2}\right)\cdot\vec{R}\times\left[n\left(\vec{r}\right)\times\vec{E}_s\left(\vec{r}\right)\right]\cdot dS' \tag{9}$$

Further refinements in (9) to include also the matrix representation (which eases the understanding of the numerical implementation) lead to:

$$\vec{E}\left(\vec{r}\right) = 2\int_S g(R)\left(\frac{ikR-1}{R^2}\right)\cdot\begin{pmatrix} 0 & z'-z & y-y' \\ z-z' & 0 & x'-x \\ y'-y & x-x' & 0 \end{pmatrix}**\begin{pmatrix} 0 & -n_z & n_y \\ n_z & 0 & -n_x \\ -n_y & n_x & 0 \end{pmatrix}*\vec{E}_s\left(\vec{r}\right)dS' \tag{10}$$

where $\vec{E}_s\left(\vec{r}\right)$ and $\vec{E}\left(\vec{r}\right)$ can be represented by the 3×1 column matrices containing the x,y,z components of the field. The first three terms form the so-called Green Tensor Matrix. Formula is enough for the computation of Directivity, and has been employed in this analysis. Alternatively, H(r) field data can also be used for the same calculations; just for completeness, the related formula, along with the formulation of the Green Tensor Matrix is:

$$\begin{cases} \overline{\overline{G}}(R) = \left(\overline{\overline{I}} + \frac{\vec{\nabla}\vec{\nabla}}{k}\right)g(R) \\ \vec{H}\left(\vec{r}\right) = -2i\omega\varepsilon\int_S \overline{\overline{G}}(R)*\begin{pmatrix} 0 & -n_z & n_y \\ n_z & 0 & -n_x \\ -n_y & n_x & 0 \end{pmatrix}*\vec{E}\left(\vec{r}\right)dS' \end{cases} \tag{11}$$

Equation (10) has been applied for each monitor and then the resulting values have been added together to compute the total field of each far point. Overall, the points have been obtained from a sphere around the structure, with a 1 m long radius. After some preliminary tests, some directions have been preferred, with the goal to reach a higher resolution of the radiation diagram in specific angles of a spherical coordinate systems.
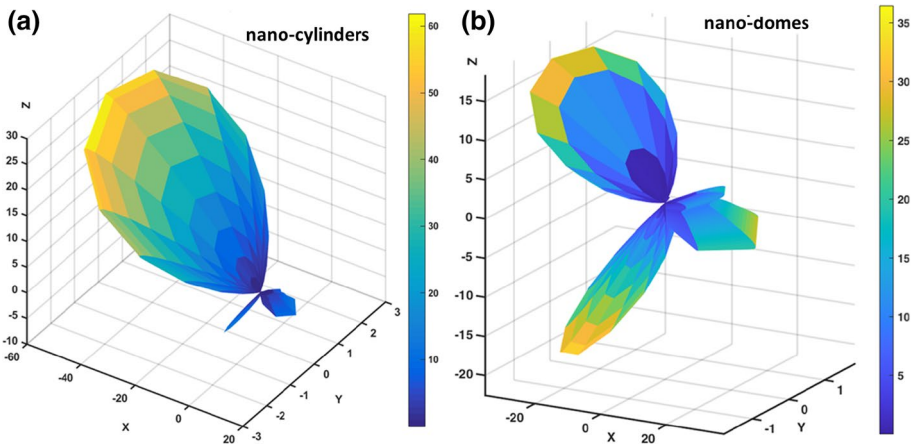

Fig. 5 Directivity of the device for **a** nano-cylinders and **b** nano-domes, as resulting from the analysis; x is the longitudinal direction, x–y is the chip plane, z=0 is the interface between top and bottom cladding
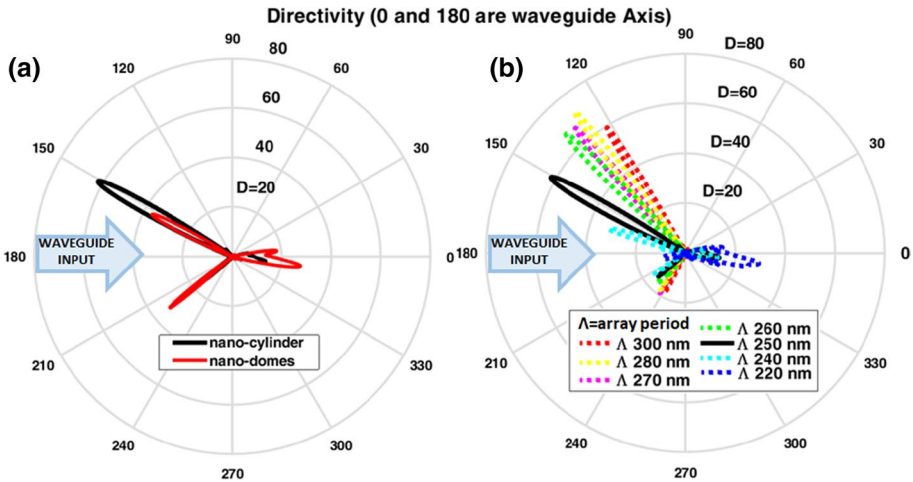
Fig. 6 2D Directivity radiation diagram along the waveguide axis: **a** comparison between nano-cylinders and nano-domes. **b** Comparison between nano-cylinders with different array periods

In Fig. 5 are shown the resulting 3D Directivity radiation diagram for both structures. As can be seen, both present similar angles in terms of main lobes, although with different directivity levels. The nano-domes display a stronger front lobe, most probably due to the higher coupling between the plasmonic mode and the guided signal.

In Fig. 6a, the 2D Directivity radiation diagram for both structures are shown, along the waveguide axis. As can be seen, the angles of the lobes in the two geometries are almost the same; this is not surprising given the same period, although slight variations can be expected if other nanostructures shapes are adopted. In Fig. 6b, the comparison between 2D Directivity radiation diagram is shown along the waveguide axis of nano-cylinders with different array periods. As can be seen, the angles vary with the separation distance. If the period is reduced, there is a higher internal reflection, corresponding to a bigger front lobe.

5 Discussion

As can be seen from Figs. 5 and 6, the periodic array gives rise to a highly collimated beam, which originates from the scattering of the feeding signal on the nano-cylinders. This can be attributed to the grating effect from the rectangular array, as suggested by Fig. 6b, where the angles can be related to the spacing between scatterers (i.e. array period). In Fig. 6a we compare the far field radiation in an array of nano-cylinders with that of nano-domes, which can be seen as an alternative structure that can be used to tune the near field radiation. It must be noted that the far field radiation angles from both structures are similar, which means that it is mostly influenced by the array characteristics.

In the context of fluorescence and Raman Scattering, setups employing our configuration can profit from this high directionality. In fact, in those systems the excitation light needs to be well separated from the emission from the molecules, and to guarantee that the two signals are often separated in time and/or space (Larkin 2017). If most of the feeding power is steered away in a direction different from the detector for the molecular emission,

in practice by employing a spatial filtering, it is possible to significantly improve emission detection performances by reducing the time gating or bandpass filtering (Hsieh et al. 2019).

While the radiation angles are dependant mainly from the array period, the optical characteristics of the overall nanoarray are more dependant from the shape of the single elements, as shown by Fig. 4. This suggests that near field design, targeted at the optimization of the molecular emission enhancement through the modeling of single structures, can be partially separated from the aforementioned excitation field management.

Also, from Fig. 2d, we notice that the excitation field is applied in-homogeneously over the array surface, as it follows the Gaussian profile of the waveguide mode in the transverse y direction, while on the longitudinal x direction it follows the profile of exponential decay. Since the relationship between the molecular emission and excitation power is linear, this characteristic can be overlooked in most applications. On the other hand, it has a significant influence in the heating of the nanoarray, which will have a similarly inhomogeneous distribution.

6 Conclusions

In this work, the main optical parameters and the far-field characteristics of a nano-array fed by a waveguide have been investigated. By comparing those with two different element geometries, nanoscopic cylinders or domes, we have obtained useful considerations and guidelines for the design of integrated optical setups for Fluorescence and Raman spectroscopy. The periodic array induces collimated and highly directional beams, which can enable spatial filtering of the excitation field, thus allowing to improve the quality of the detection of molecular emission. The optimization of the emission enhancement, which involves the modeling of the single elements, did not perturbate significantly spatial filtering.

In order to analyze this type of configurations, some approximations to the scattering theory were adopted. Those have been outlined, along with the procedure used to compute the far field.

Overall, our results show that the integration of the spectroscopic setups may yield also advantages in terms of performance, in addition to the easier handling and long term cost reduction. While the study of this type of schemes requires further analyses, in particular in the near-field interactions, our methods, results and guidelines can be useful tools for the development of this complex integrated system for Fluorescence and Raman spectroscopy.

References

Alam, B., Ferraro, A., d'Alessandro, A., Caputo, R., and Asquini, R.: Optical properties of a waveguide-fed plasmonic nano-array through approximated scattering theory. In: IEEE International Conference on Numerical Simulation of Optoelectronic Devices (NUSOD), 23–24 (2021).

Asquini, R., Buzzin, A., Caputo, D., de Cesare, G.: Integrated evanescent waveguide detector for optical sensing. IEEE Trans. Components, Packag. Manuf. Technol. **8**, 1180–1186 (2018). https://doi.org/10.1109/TCPMT.2018.2818946

Balanis, C.A.: Antenna Theory: Analysis and Design, 4th Edition. Wiley (2016). ISBN: 978-1-118-64206-1

Benedetti, A., Belardini, A., Veroli, A., Centini, M., Sibilia, C.: Numerical tailoring of linear response from plasmonic nano-resonators grown on a layer of polystyrene spheres. J. Appl. Phys. **116**, 164312 (2014). https://doi.org/10.1063/1.4900992

Bohren, C. F., Huffman, D.R.: Absorption and Scattering of Light by Small Particles, chapter 3. John Wiley & Sons, 57–129 (1983).

Buzzin, A., Asquini, R., Caputo, D., de Cesare, G.: On-glass integrated SU-8 waveguide and amorphous silicon photosensor for on-chip detection of biomolecules: feasibility study on hemoglobin sensing. Sensors **21**(2), 415 (2021). https://doi.org/10.3390/s21020415

Calò, G.; Alam, B.; Bellanca, G.;Fuschini, F.; Barbiroli, M.; Tralli, V.; Bassi, P.; Stomeo, T.; Bozzetti, M.; Kaplan, A.E, Shafiei Dehkordi, J., Zoli, M., Nanni, J., Petruzzelli, V.: Dielectric and Plasmonic Vivaldi Antennas for On-Chip Wireless Communication. In: 21st International Conference on Transparent Optical Networks (ICTON), 1–4 (2019). https://doi.org/10.1109/ICTON.2019.8840426

Centini, M., Benedetti, A., Larciprete, M.C., Belardini, A., Li Voti, R., Bertolotti, M., Sibilia, C.: Midinfrared thermal emission properties of finite arrays of gold dipole nanoantennas. Phys. Rev. B **92**, 205411 (2015)

Choi, C., Xu, Z., Wu, H.Y., Liu, L., Cunningham, B.: Surface-enhanced Raman nanodomes. Nanotechnology **21**(41), 415301 (2010). https://doi.org/10.1088/0957-4484/21/41/415301

Dhakal, A., Peyskens, F., Clemmen, S., Raza, A., Wuytens, P., Zhao, H., Le Thomas, N., Baets, R.: Single mode waveguide platform for spontaneous and surface-enhanced on-chip Raman spectroscopy. Interface Focus **6**, 20160015 (2016). https://doi.org/10.1098/rsfs.2016.0015

Hsieh, C., Verma, M., Liu, Q.: Improving depth sensitive fluorescence spectroscopy with wavefront shaping by spectral and spatial filtering. IEEE Access **7**, 170192–170198 (2019). https://doi.org/10.1109/ACCESS.2019.2955564

Kasani, S., Curtin, K., Wu, N.: A review of 2D and 3D plasmonic nanostructure array patterns: fabrication, light management and sensing applications. Nanophotonics **8**(12), 2065–2089 (2019). https://doi.org/10.1515/nanoph-2019-0158

Larkin, P. J.: Infrared and Raman Spectroscopy, Principles and Spectral Interpretation, 2nd Edition. Elsevier (2017). ISBN: 9780128041628

Mahi, N., Lévêque, G., Saison, O., Marae-Djouda, J., Caputo, R., Gontier, A., Maurer, T., Adam, P.M., Bouhafs, B., Akjouj, A.: In Depth Investigation of lattice plasmon modes in substrate-supported gratings of metal monomers and dimers. J. Phys. Chem. C **121**(4), 2388–2401 (2017). https://doi.org/10.1021/acs.jpcc.6b11321

Maier, S.A.: Plasmonics: Fundamentals and Applications. Springer, NY (2010)

Martin, O.J.F., Piller, N.B.: Electromagnetic scattering in polarizable backgrounds. Phys. Rev. E **58**, 3909–3915 (1998). https://doi.org/10.1103/PhysRevE.58.3909

Stratton, J.A., Chu, L.J.: Diffraction theory of electromagnetic waves. Phys. Rev. **56**, 99–107 (1939). https://doi.org/10.1103/PhysRev.56.99

Sultangaziyev, A., Bukasov, R.: Review: Applications of surface-enhanced fluorescence (SEF) spectroscopy in bio-detection and biosensing. Sensing and Bio-Sensing Research **30**, 100382 (2020). ISSN 2214-1804, https://doi.org/10.1016/j.sbsr.2020.100382

Thomas, S., Grohens, Y., Vignaud, G., Kalarikkal, N., James, J.: Nano-optics. Elsevier (2020). https://doi.org/10.1016/C2018-0-02751-6

Tian, Y., Wang, H., Xu, W., Liu, Y., Xu, S.: Waveguide-coupled localized surface plasmon resonance for surface-enhanced Raman scattering: Antenna array as emitters, Sensors and Actuators B: Chemical **280**, 144–150 (2019). ISSN 0925-4005, https://doi.org/10.1016/j.snb.2018.10.028

Veroli, A., Alam, B., Maiolo, L., Todisco, F., Dominici, L., De Giorgi, M., Pettinari, G., Gerardino, A., Benedetti, A.: High circular dichroism and robust performance in planar plasmonic metamaterial made of nano-comma-shaped resonators. J. Opt. Soc. Am. B **36**(11), 3079–3084 (2019). https://doi.org/10.1364/JOSAB.36.003079

Yu, H., Peng, Y., Yang, Y., Li, Z.Y.: Plasmon-enhanced light–matter interactions and applications. NPJ Comput Mater **5**, 45 (2019). https://doi.org/10.1038/s41524-019-0184-1

Zou, J., Zhao, F., Chen, R.T.: Two-step K+-Na+ and Ag+-Na+ ion-exchanged glass waveguides for C-band applications. Appl. Opt. **41**(36), 7620–7626 (2002). https://doi.org/10.1364/AO.41.007620